PCCP

ROYAL SOCIETY OF CHEMISTRY

PAPER

View Article Online
View Journal

Cite this: DOI: 10.1039/d3cp01070h

Description of quantum interference using mixed quantum/classical theory of inelastic scattering†

Dulat Bostan, Bikramaditya Mandal, Carolin Joy and Dmitri Babikov *

Manifestation of the quantum interference effect in the oscillation of scattering cross section is explored using the N_2 + O system as a case study. Calculations are carried out for two electronic PESs of the system, for various initial rotational states of N_2, in a broad range of N_2 + O collision energies and using three theoretical methods: two versions of the approximate mixed quantum/classical theory (MQCT and AT-MQCT) and the accurate full-quantum coupled-channel method (implemented in MOLSCAT). A good agreement between different methods is observed, especially at high energies. Elastic scattering cross-sections oscillate as a function of collision energy, which is the result of quantum interference. The effects of initial rotational excitation and of the PES properties are studied in detail. For the final (thermally averaged) cross sections, both MOLSCAT and MQCT calculations predict a rather regular pattern of quantum oscillations that persist through a broad range of collision energies and expand into the low-energy regime where quantum scattering resonances are common. The difference between cross sections predicted by MQCT and MOLSCAT decreases from ~8% at low energies to ~2% at high energies. Experimental data available at high collision energies are well reproduced.

Received 7th March 2023,
Accepted 12th May 2023

DOI: 10.1039/d3cp01070h

rsc.li/pccp

I. Introduction

The quantum interference effect originates in the scattering phase shift[1–5] and manifests as two distinct phenomena prominent in the inelastic scattering. One of them is oscillation of differential cross section as a function of the scattering angle, known as quantum glory and observed in the narrow range near the forward scattering direction.[6–8] Another related phenomenon is oscillation of integral cross section as a function of collision energy.[9–13] The focus of this paper is on the later phenomenon, observed in a broad range of collision energies including the high energy scattering regime (which is different from sharp resonances observed in the narrow range of low collision energies only).[14–16]

In recent years we saw a revival of interest in the quantum interference effects.[4,6,17,18] This is in part due to the development of experimental techniques that permit one to probe quantum glory in the lab,[6] and in part due to the applied interest in scattering cross sections for atmospheric species, important in such applications as the atmospheric re-entry problem[19] or the air-breathing propulsion system of low-orbit satellites.[17,18,20] Interestingly, two recent theoretical treatments[6,17,18] of these phenomena employed an approximate description of molecular scattering that combines classical and quantum mechanics.

In particular, inelastic scattering in the N_2 + O(^{3}P) system was recently studied[17,18] using two theoretical methods. First, an infinite order sudden (IOS) method,[21,22] which is an approximate quantum method, was used to describe oscillations of scattering cross section observed in the earlier experimental work.[9] Next, the quantum classical theory of Billing, in which only the vibrational motion is described by quantum mechanics, while the rotational and translational degrees of freedom are treated classically,[23,24] was used to determine the rate of quenching of vibrationally excited $N_2(v = 1)$ to the ground vibrational state, by collisions with O(^{3}P). This process is important in the upper atmosphere, where atomic oxygen represents the second major species after molecular nitrogen, and thus plays a key role in the energy transfer process (*e.g.*, in the high-temperature shock wave near the surface of spacecraft or hypersonic aircraft).[25–27]

In this paper we present a rigorous study of the same molecular system, N_2 + O(^{3}P), using two alternative theoretical tools, that may offer some improvement over the previous work. Namely, we carried out accurate quantum calculations of cross section oscillations using the time-independent coupled-channel (CC) method which, if numerically converged and combined with an accurate potential energy surface (or surfaces and surface couplings, in a nonadiabatic process),[5] is usually considered to offer a nearly exact treatment of the process. In these calculations we covered a broader range of collision energies, compared to the previous work, which permitted us to see better the oscillations of cross section as a function of

Chemistry Department, Marquette University, Milwaukee, Wisconsin 53201-1881, USA. E-mail: dmitri.babikov@mu.edu

† Electronic supplementary information (ESI) available: A set of additional Fig. S1–S11 as described in the text. See DOI: https://doi.org/10.1039/d3cp01070h

energy. Then, we repeated all the same calculations using our mixed quantum/classical theory (MQCT) code.[28,29] In MQCT, both the rotational and vibrational degrees of freedom in N_2 are treated quantum mechanically using the time-dependent Schrödinger equation, and only the translational motion responsible for N_2 + O scattering is treated approximately using mean-field trajectories. Since in this work the focus is on the individual rotational state-to-state transitions at low energies, and their effect on the oscillation of cross section as a function of collision energy, MQCT is expected to offer a more detailed description compared to the method of Billing, where the rotational states are not quantized, and the rotational motion is treated classically. At the early state of this work, we carried out MQCT calculations with both rotational and vibrational states taken into consideration and found that, in the energy range covered by the experiment,[9] the population of excited vibrational states remains negligibly low. Therefore, in the calculations reported here, both MQCT and MOLSCAT, only the ground vibrational state $v = 0$ was included in the basis. Still, a 3D potential energy surface of N_2 + O was used, without any dimensional reduction, with rotational state-to-state transition matrix elements averaged over the vibrational coordinate (N_2 diatomic bond distance). This was done using SYS_TYPE = 2 capability of both MQCT and MOLSCAT programs, which is a vibrating-rotor system type. For both programs, only the inter-molecular part of the interaction potential was supplied as input, while the intra-molecular potential of an isolated N_2 was removed. Such potential has no dependence on the bond length of N_2 in the asymptotic range (when the O atom is at infinity) but when the O atom is brought up closer to interact with the N_2 molecule, the compression or stretching of the N_2 bond still leads to the change of potential energy of the system. As explained above, this interaction is averaged over the vibrational wavefunction(s) when the matrix elements are computed. The actual calculations of vibrational excitation and quenching in high-energy N_2 + O collisions are ongoing and will be reported elsewhere.

Another goal was to test the performance of MQCT for the description of the quantum interference effect, by comparing its results against the accurate quantum CC results and against the IOS results from the previous work,[17] using the same potential energy surface. This is important, because MQCT permits one to carry out calculations for larger and heavier molecules[29–34] and at higher collision energies than it is possible with any other codes available in the inelastic scattering community now, and thus represents a promising new tool. Moreover, MQCT can provide a unique time-dependent insight into the process,[30,35] not available from the standard time-independent quantum methods.

II. Theoretical framework

The most general form of MQCT equations of motion, applicable to the collision of two asymmetric-top rotor molecules, has been presented in the recent literature.[29,31] Here, for the sake of completeness, we present a summary of MQCT equations for rotational state-to-state transitions in the diatom + atom system such as N_2 + O, which is the simplest case. All relevant derivations can be found in the literature.[36,37]

In MQCT, the rotational motion of a diatomic molecule is described by polar and azimuthal angles θ and φ measured relative to the body-fixed reference frame – a rotating frame tied to the molecule-atom vector $\vec{R}$. These two angles are quantum degrees of freedom, and their evolution is determined by the wave function $\psi(\theta,\varphi,t)$ expanded over the basis set of rotational eigenstates $Y_{jm}(\theta,\varphi)$ using time-dependent coefficients $a_{jm}(t)$ as follows:

$$\psi(\theta,\varphi,t) = \sum_{jm} a_{jm}(t)\, Y_{jm}(\theta,\varphi) \exp\{-iE_j t\} \tag{1}$$

Here m is the projection of angular momentum j of the molecule onto the molecule-atom axis $\vec{R}$, which plays the role of the quantization axis in the body-fixed reference frame. The energy E_j of an eigenstate depends on j only and does not depend on m. Equations for time evolution of probability amplitudes $a_{jm}(t)$ are obtained by substitution of eqn (1) into the time dependent Schrodinger equation, which gives[36,37]

$$\begin{aligned} \dot{a}_{jm} \;=\; & -i\sum_{j'} a_{j'm} M^{j}_{j'm} \mathrm{e}^{i\varepsilon^{j}_{j'}t} \\ & -\dot{\Phi}\Big[a_{j,m-1}\sqrt{j(j+1)-m(m-1)} \\ & +a_{j,m+1}\sqrt{j(j+1)-m(m+1)}\Big]\Big/2 \end{aligned} \tag{2}$$

Summation in the first term of this equation includes quantum state-to-state transitions, within given m, driven by potential coupling matrix $M^{j}_{j'm}$ that depends parametrically on the molecule-atom distance R. This matrix is real-valued, time-independent and is diagonal in m:

$$M^{j}_{j'm}(R) = \big\langle Y_{jm}(\theta,\varphi)\big|V(\theta,R)\big|Y_{j'm}(\theta,\varphi)\big\rangle. \tag{3}$$

In eqn (2) $\varepsilon^{j}_{j'}$ correspond to energy differences between the final (upper index) and the initial (lower index) rotational states of the system with energies E_j and $E_{j'}$, respectively. The second term in eqn (2) describes transitions between the rotational states with $\Delta m = \pm 1$, driven by classical orbital angular velocity $\dot{\Phi}$ of vector $\vec{R}$ rotation, which is the Coriolis coupling effect. Time evolution of classical degrees of freedom, R and Φ, and their conjugate momenta P_R and P_Φ, is described by the following equations, obtained using the Ehrenfest theorem:[36,37]

$$\dot{R} = \frac{P_R}{\mu} \tag{4}$$

$$\dot{\Phi} = \frac{P_\Phi}{\mu R^2} \tag{5}$$

$$\dot{P}_R = -\sum_{j'}\sum_{j''} \mathrm{e}^{i\varepsilon^{j''}_{j'}t} \sum_{m} \frac{\partial M^{j''}_{j'm}}{\partial R} a^{*}_{j''m} a_{j'm} + \frac{P_\Phi{}^2}{\mu R^3} \tag{6}$$

$$\begin{aligned}\dot{P}_\Phi &= -i\sum_{j'}\sum_{j''} e^{i\omega_{j'}^{j''}t}\sum_m M_{j'm}^{j''} \\ &\times\Big[a^*_{j''m-1}a_{j'm}\sqrt{j''(j''+1)-m(m-1)} \\ &+ a^*_{j''m+1}a_{j'm}\sqrt{j''(j''+1)-m(m+1)} \\ &- a^*_{j''m}a_{j'm-1}\sqrt{j'(j'+1)-m(m-1)} \\ &- a^*_{j''m}a_{j'm+1}\sqrt{j'(j'+1)-m(m+1)}\Big]\Big/2\end{aligned} \tag{7}$$

The triple sum in eqn (6) and (7) represents the average effect of all rotational states (j,m) of the molecule on the scattering of the atom.

In a straightforward realization of MQCT the equations for quantum and classical degrees of freedom (eqn (1) and (2) and (4)–(7), respectively) are propagated simultaneously in a coupled manner, as one system of differential equations. In this case the major numerical cost is associated with the estimation of the triple sum in the right-hand side of eqn (6) and (7) for classical momenta P_R and P_Φ. A numerically efficient approximation is obtained by decoupling the classical and quantum degrees of freedom, in which case we first propagate eqn (4)–(7) for classical trajectories adiabatically, keeping only the initial state in the basis set (one j-state with all associated m-components), and then, in a consecutive run, we propagate eqn (1) and (2) for quantum probability amplitudes, using the full basis set of rotational states (j,m). This method, named adiabatic-trajectory, or AT-MQCT,[29,32,35] gives results similar to MQCT at a reduced cost.

In any case, we set $a_{jm} = 1$ for a chosen initial state (j,m) at the initial moment of time and propagate MQCT trajectories through the interaction region to determine the final $a^{(\ell)}_{j'm'}$, where ℓ is the orbital angular momentum quantum number closely related to the collision impact parameter b through $\ell(\ell+1) = k^2b^2$. The absolute value of the initial momentum $\mathbf{P} = \hbar\mathbf{k}$ is determined by collision energy, $P = \sqrt{2\mu U}$, while the direction of $\mathbf{P}$ in space is determined by ℓ. In order to define the P_R and P_Φ components of $\mathbf{P}$, the value of ℓ is sampled between 0 and $\ell_{\max}$ and is used to define the initial classical momentum $P_\Phi = \hbar\sqrt{\ell(\ell+1)}$ in eqn (5) and (6). The value of P_R to use in eqn (4) is computed from $P_R{}^2 = \mathbf{P}^2 - P_\Phi{}^2/R^2$. Inelastic cross sections are calculated from a set of MQCT trajectories for $0 \le \ell \le \ell_{\max}$ as[16]

$$\sigma_{jm\to j'} = \frac{\pi}{k^2}\sum_{\ell=0}^{\ell_{\max}}(2\ell+1)p_{j'}^{(\ell)}, \tag{8}$$

where the total transition probability $p_{j'}^{(\ell)}$ for each channel j' is obtained from final probability amplitudes $a^{(\ell)}_{j'm'}$ as a sum over all final states m' of the channel:

$$p_{j'}^{(\ell)} = \sum_{m'=-j'}^{+j'}\left|a^{(\ell)}_{j'm'}\right|^2 \tag{9}$$

Survival probability $p_j^{(\ell)}$ for the initial channel is computed using a formula analogous to eqn (9) but with all unprimed indexes, and is used to obtain the elastic scattering amplitude $A^{(\ell)} = \sqrt{p_j^{(\ell)}}$ and cross section:

$$\sigma_{jm\to j} = \frac{\pi}{k^2}\sum_{\ell=0}^{\ell_{\max}}(2\ell+1)\left(1 - A^{(\ell)}e^{i\delta(\ell)}\right)^2 \tag{10}$$

where the phase shift $\delta(\ell)$ is obtained by integration of the deflection function $\chi(\ell)$, starting from the asymptotic region where the phase shift is zero:

$$\delta(\ell) = \int_{\ell_{\max}}^{\ell}\chi(s)\mathrm{d}s \tag{11}$$

Transition and survival probabilities $p_{j'}$ and p_j, the deflection angle χ and the phase shift δ all depend on the initial rotational state jm, but this dependence is omitted in eqn (8)–(11) for clarity. The final cross sections $\sigma_{j\to j'}$ (including the one for elastic channel $j' = j$) are obtained as average over the initial m:

$$\sigma_{j\to j'} = \frac{1}{2j+1}\sum_{m=-j}^{+j}\sigma_{jm\to j'}. \tag{12}$$

Inelastic cross section σ_j is obtained as a sum of $\sigma_{j\to j'}$ over final $j' \neq j$. The total cross section is a sum of inelastic and elastic cross sections.

In the calculations presented below we took a large basis set of rotational states up to $j = 20$ and considered the initial states up to $j = 10$. Since cross sections change smoothly as a function of the initial j, and since N_2 is a homonuclear diatomic molecule with odd Δj transitions forbidden, we carried out calculations with only even j-values included. Elements of the state-to-state transition matrix were computed numerically using Gauss–Legendre quadrature in θ with 40 points (integration over φ is analytic, since PES does not depend on φ). Cubic spline was used to interpolate the values of matrix elements between the points of radial grid, which included 100 points in the range $4.0 \le R \le 50$ Bohr using logarithmic step-size. The equations of motion, eqn (1), (2) and (4)–(7), were propagated using the 4th-order Runge–Kutta method with a step size of $t = 10$ a.u. Our trajectories start at $R_{\max} = 50$ Bohr with impact parameters up to $b_{\max} = 40$ Bohr which corresponds to $\ell_{\max} \sim 60$ at low collision energy and $\ell_{\max} \sim 900$ at high collision energy. These large values of $b_{\max}$ and $\ell_{\max}$ were needed to reach the convergence of elastic cross sections within 1% of their values. Inelastic cross sections could in principle be computed with smaller values of $b_{\max}$ and $\ell_{\max}$.

For quantum CC calculations, we used the standard code MOLSCAT[21,22] with the same rotational basis set, $R_{\max} = 50$ Bohr with step size parameter DR = 0.04, 41 grid points for integration over the θ angle, and the number of partial scattering waves up to $J_{\text{tot}} \sim 40$ at low collision energy and $J_{\text{tot}} \sim 500$ at high collision energy. The PES was expanded using 11 even terms up to $\lambda = 20$. MOLSCAT calculations showed convergence properties very similar to those of MQCT, with all cross sections converged within 1%. It appears that the values of elastic cross sections are quite sensitive to Rmax; therefore, a relatively large value of molecule–atom separation was needed in both MQCT

and MOLSCAT calculations. The effect of neglecting the excited vibrational states is also estimated to be within 1%. Thus, one can conduct a direct one-to-one comparison of our MQCT and MOLSCAT results.

For both MQCT and MOLSCAT, thermally averaged cross sections $\sigma_{ave}(T)$ were obtained as

$$\sigma_{ave}(T) = \sum_j w_j(T)\sigma_j \quad (13)$$

using the following weights and partition function:

$$w_j(T) = (2j+1)e^{-\frac{E_j}{kT}}/Q(T), \quad (14)$$

$$Q(T) = \sum_j (2j+1)e^{-\frac{E_j}{kT}}. \quad (15)$$

We found that the values of σ_j vary smoothly with j. For this reason, the effect of explicit inclusion of odd j states into $\sigma_{ave}(T)$ is insignificant, within 1% the of cross section value. Therefore, thermal averaging was done with even states only. At T = 90 K, which corresponds to experimental conditions of ref. 9, the rotational state with j = 4 has the highest weight.

The effect of electronic states on the process of $N_2 + O(^3P)$ scattering is described approximately using two potential energy surfaces introduced in ref. 17 and labeled in that work as Σ and Π. Scattering calculations are done independently on these two PESs and the resultant cross sections are averaged using statistical weights that correspond to the high-temperature source of $O(^3P)$ atoms in the experiment,[9] namely, Σ/Π = 1/2 (see ref. 17 and 18).

III. Results

Individual state-to-state transition cross sections, that include excitation, quenching, and elastic channels, were computed for the initial rotational states j = 0, 2, 4, 6, 8 and 10 in the range of collision energies from 30 to 3000 cm^{-1}. All these data are presented in the ESI† in Fig. S1 and S3 for Π PES, and in Fig. S2 and S4 (ESI†) for Σ PES. In Fig. S1 and S2 (ESI†) we have compared the results of full-coupled MQCT calculations against MOLSCAT, while in Fig. S3 and S4 (ESI†) we have compared the results of decoupled AT-MQCT against MOLSCAT. Some of these data are presented in Fig. 1. From these figures one can see a generally good performance of MQCT methods in a broad range of collision energies and through several orders of magnitude of cross section values. In all cases MQCT predicts correct threshold behavior for excitation processes and shows no threshold for quenching processes. At high collision energies the results of MQCT become very close to the full-quantum MOLSCAT results. At low collision energies, dominated by quantum scattering resonances, and for small cross sections near threshold, one can see some differences between the full-quantum results and MQCT results, which is expected, taking into consideration the classical nature of MQCT trajectories.

Inelastic (summed over the final rotational states j') and elastic cross sections computed from MQCT and MOLSCAT data are presented in Fig. 2 for different initial rotational states up to j = 10 and for both PESs of the N_2 + O system. Fig. S5 in the ESI† reports similar data obtained by AT-MQCT. By comparing different frames of these figures we confirm once again that MQCT methods offer a viable description of inelastic scattering, giving cross sections that are very similar to the results of the full-quantum CC method. In particular, from Fig. 2 we see that the energy dependence of inelastic cross sections is reproduced very well by MQCT on both PESs of N_2 + O. For all cases, the value of inelastic cross section is the largest for the ground rotational state j = 0 (blue line in Fig. 2), it decreases quickly as we move to j = 2 (orange line in Fig. 2) and then keeps decreasing further (but at a slower rate) as we move to j = 4 and above. We also see that the values of inelastic cross sections for j = 0 are somewhat larger on Σ PES than those on Π PES. In contrast, the values of inelastic cross sections for j = 2 and higher are comparable on two PESs, but those on Π PES tend to decrease or remain the same as a function of collision energy, while those on Σ PES tend to increase with energy. Both MQCT (in Fig. 2) and AT-MQCT (in Fig. S5, ESI†) methods reproduce these features well.

The behavior of elastic cross sections is very different. Their magnitudes are larger than those of inelastic cross sections by a factor ranging from 3 to 10, and they grow as the value of j is raised (see Fig. 2 and Fig. S5, ESI†). At low collision energies,

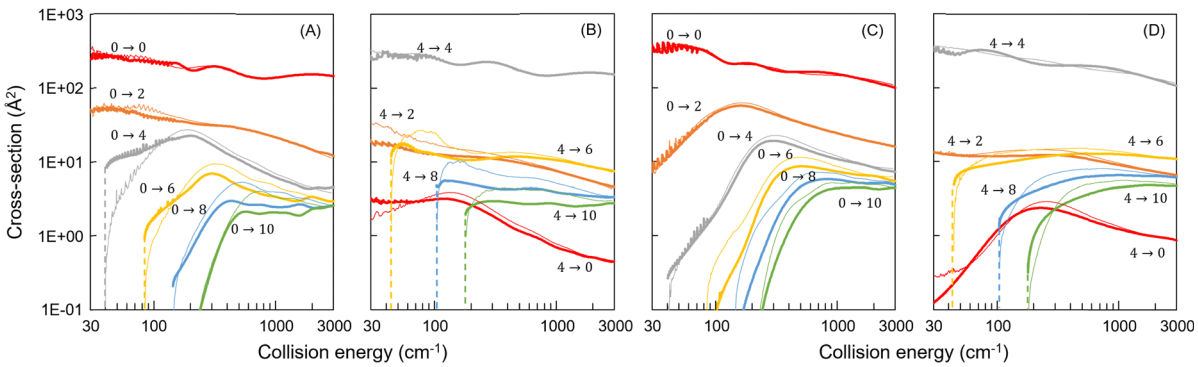

Fig. 1 State-to-state transition cross sections from the initial states j = 0 and j = 4 to several final states j' using two PESs for the N_2 + O system: Π PES (frames A and B) and Σ PES (frames C and D). The thick lines correspond to MQCT results, while the thin lines are MOLSCAT results. The dashed lines are used to indicate threshold energies of excitation transitions.

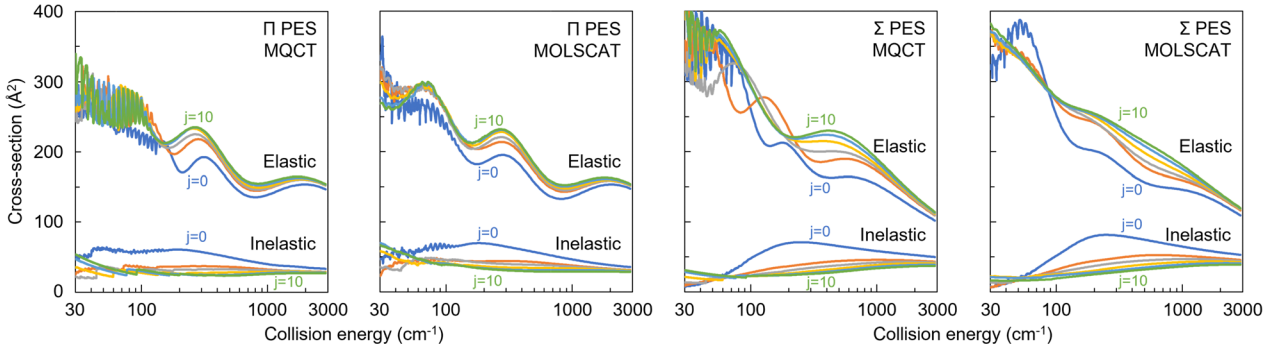

Fig. 2 Elastic and inelastic cross sections as a function of collision energy obtained by MQCT and MOLSCAT methods for different initial states of the N_2 + O system indicated by colors: j = 0 is blue, j = 2 is orange, j = 4 is gray, j = 6 is yellow, j = 8 is turquoise and j = 10 is green. The left two frames correspond to Π PES, while the right two frames correspond to Σ PES.

elastic cross sections exhibit many scattering resonances seen as sharp spikes in the energy dependence, and these are present in both MQCT and MOLSCAT results. In the case of Σ PES resonances disappear at 80 cm^{-1} or so, while in the case of Π PES they persist up to 140 cm^{-1}. Importantly, the values of elastic cross sections oscillate as a function of energy, and these oscillations are more regular in the case of Π PES where they occur for all values of j, compared to Σ PES where the increase of j leads to some suppression of elastic cross section oscillations (see Fig. 2).

Since the elastic cross sections increase but the inelastic cross sections decrease as j is raised, one may wonder how sensitive the value of total cross section (elastic + inelastic) would be to the variations of j. One example is given in Fig. 3 (for Π PES) that demonstrates that these two trends largely cancel, making the total cross section barely sensitive, and more so at high collision energy where it becomes insensitive, to the initial rotational excitation. The results for Σ PES and the data obtained using AT-MQCT are presented in Fig. S6 of the ESI,† and they show a similar effect.

Due to the fact that the dependence of total cross section on the initial rotational excitation j is weak, the behavior of thermally averaged cross sections (computed as a weighted sum over j) happens to look very similar to that shown in Fig. 2 and 3. For completeness, we have presented energy dependencies of thermally averaged cross sections in Fig. S7 (ESI†), obtained using three theoretical methods (MOLSCAT, MQCT and AT-MQCT) for two PESs of the N_2 + O system (Σ and Π). Here, in Fig. 4, we have plotted the same data but in a different way.

In Fig. 4 we plot the product $\sigma_{ave} \times v^{2/5}$ as a function of the incident velocity of O-atom $v = \sqrt{2E/\mu}$, where E is the energy of collision in the center-of-mass reference frame while μ is the reduced mass of the molecule–quencher system. This choice of variables compensates for the dependence of elastic cross section on collision energy and makes its oscillations visible better.[9,10,17,18] From this figure we can see that in the case of Π PES (upper row of frames in Fig. 4) all three theoretical methods give very similar patterns of cross section oscillations, and, in the adopted energy window, one can observe oscillations of two and a half periods. Interestingly, this trend extends into the low-energy

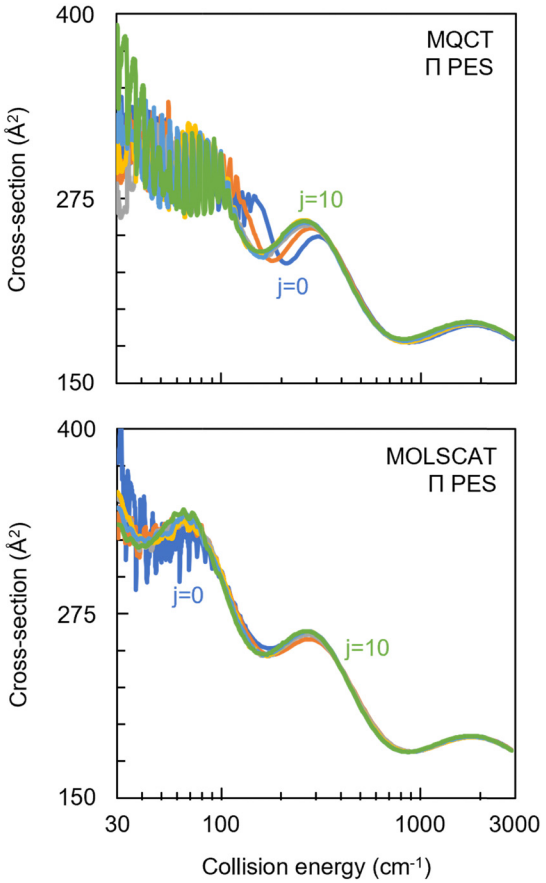

Fig. 3 Total cross sections (elastic + inelastic) as a function of collision energy computed using MOLSCAT and MQCT for the initial states $0 \leq j \leq 10$ of the N_2 + O system using Π PES. Colors are the same as in Fig. 2.

regime, where scattering resonances are abundant but lead to a relatively small jiggling of the oscillating curve. In a sense, quantum scattering resonances have a minor effect on major quantum oscillations of elastic scattering cross section, and this behavior is captured by both MOLSCAT and MQCT methods.

Finally, using thermally averaged cross sections for Σ and Π PESs of the N_2 + O system from Fig. 4, we computed the overall

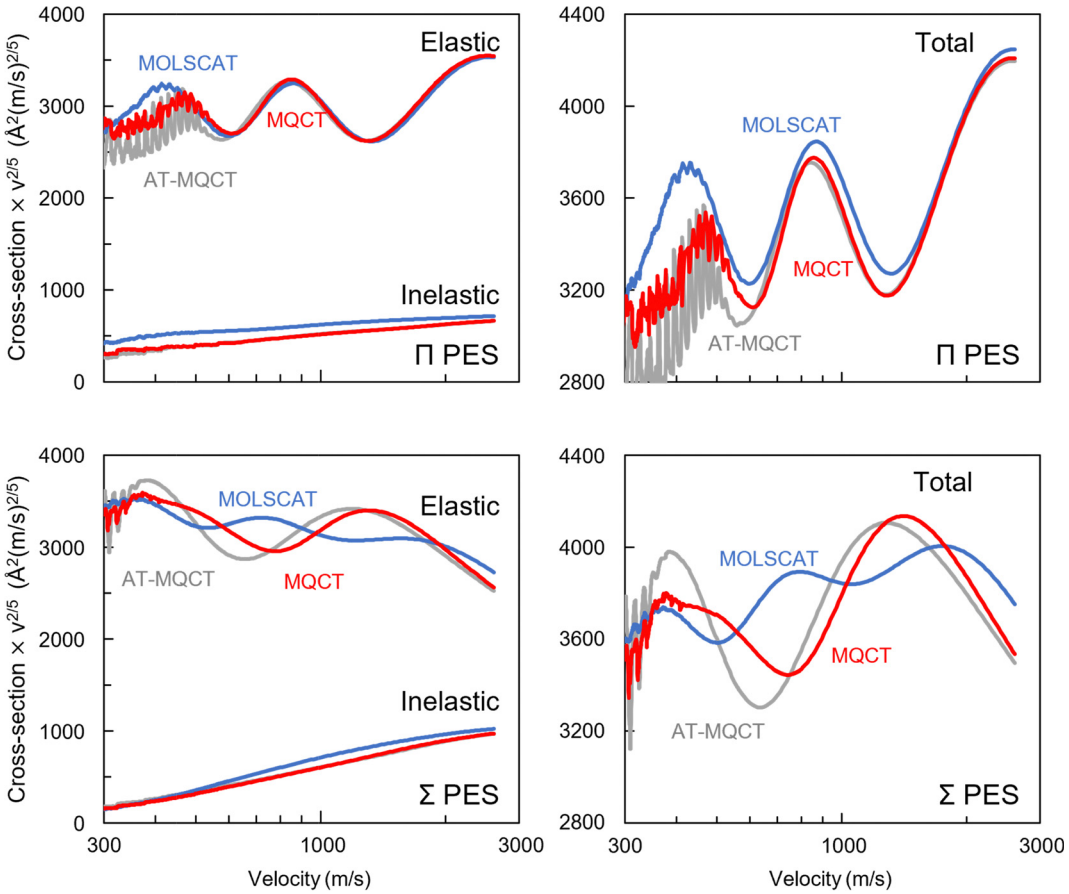

Fig. 4 Velocity scaled cross sections as a function of average collision velocity obtained by three theoretical methods, as indicated by color. Left panels – elastic and inelastic cross-sections, right panels – total cross-sections. The upper and lower rows correspond to Π and Σ PESs of the N_2 + O system, respectively.

scattering cross section, which is a weighted sum of total cross sections for Σ and Π. Our results obtained by MOLSCAT and MQCT methods are presented in Fig. 5, where they are compared with the results of an approximate IOS method from the literature[17] and the available experimental data[9] (as included in Fig. 1 of the recent paper by Hong[17]). Since the Σ to Π ratio is 1 to 2 (see Section II), the main contribution comes from Π PES, and the overall cross section appears to look quite similar to that of Π PES (compare Fig. 5 *vs.* Fig. 4), namely, two and a half periods of cross section oscillations are observed in the chosen range of collision velocities, and this behavior is captured correctly by the MQCT method, in very good agreement with MOLSCAT results through the entire range of collision velocities (energies). The MQCT method underestimates the value of overall cross section slightly: by ∼2% at high energy, ∼5% in the middle of the range, and ∼8% at low energy. Resonances at low energy play a minor role and do not obscure the major oscillations of cross section that expand into the low energy range (see Fig. 5). In contrast, the IOS approximation reproduces less than one period of cross section oscillations at high energy only and goes to a plateau in the middle of the range, which is incorrect. This is because the IOS approximation is expected to be accurate at high energy but may fail at low energy, which is exactly what we observe here. However, experimental

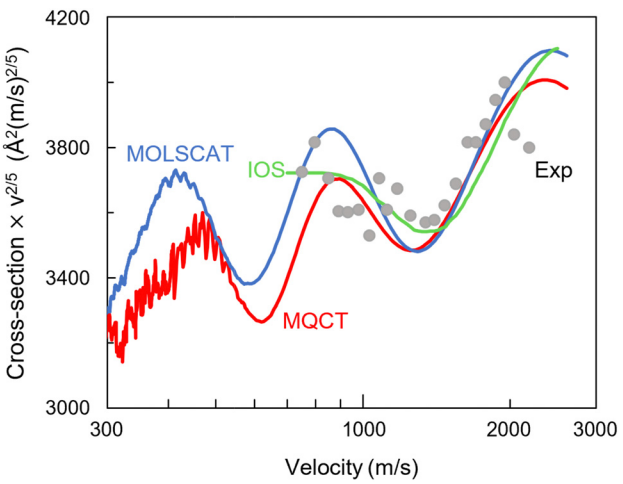

Fig. 5 Velocity-scaled cross sections as a function of O-atom collision velocity. The red line is MQCT results, the blue line is MOLSCAT results, the green line is IOS approximation from the literature, and the grey dots are experimental data.

data, available at higher collision energies only, are reproduced well by all three theoretical methods: the coupled-channel

method of MOLSCAT, our MQCT method, and the IOS method from the literature. It should be noted that experimental error bars vary in the range from 20 to 50% of the oscillation amplitude.[9]

IV. Discussion

Let's analyze the results presented in Fig. 4 in more detail. In the case of Π PES both the amplitude and the period of elastic cross section oscillations are reproduced well by MQCT. At high energy and in the middle of the interval, MQCT cross section for the elastic process is smaller than that of MOLSCAT barely by ~1% of the cross section value. This difference becomes larger (~7%) at low energies where scattering resonances are common. Importantly, oscillations of the total scattering cross section come entirely from the elastic process since the behavior of inelastic cross section is very monotonic (according to both MOLSCAT and MQCT data).

In the case of Σ PES (lower row of frames in Fig. 4) we see many same features, except that the difference between predictions of MOLSCAT and MQCT becomes more substantial. In particular, MQCT predicts larger amplitude and larger period of cross section oscillations, compared to MOLSCAT. Namely, in the adopted energy window we observe three periods of cross section oscillations according to MOLSCAT, but only two periods according to MQCT. The amplitude of oscillations for the elastic process is about 8% of the cross section value according to MOLSCAT, but it reaches 17% in the case of MQCT (which is similar to the case of Π PES, where the amplitude of elastic cross section is ~22%). The behavior of inelastic cross sections in Fig. 4 is also different for two PESs of N_2 + O. Namely, on Π PES the inelastic cross section changes very little as a function of collision velocity (or energy), while on Σ PES it shows a substantial and steady growth.

The difference of MQCT predictions on two PESs of the same N_2 + O system (same mass of collision partners, same spectra of rotational states) must be related to different landscapes of potential energy. Indeed, in ref. 17, where these PESs were constructed, it was shown that

(1) in the T-shaped configuration the well depth of Σ PES is almost the same as that of Π PES; and

(2) in the collinear configuration Σ PES has no attractive interaction whatsoever, while Π PES exhibits attraction for all configurations.

This gives us a hint that, on average, Σ PES may be more anisotropic than Π PES. To compare the two PESs in a more quantitative way, we expanded them over a set of Legendre polynomials.[29] Radial dependencies of expansion coefficients are presented in Fig. S8 of the ESI.† These data indicate that, first of all, the isotropic interaction term $v_0(R)$ is more than twice smaller for Σ PES than for Π PES. Second, in the case of Σ PES, the quadrupole interaction term is repulsive through the entire range, $v_2(R) > 0$, and is comparable in magnitude to the isotropic term, $|v_2(R)| \sim |v_0(R)|$. Due to this feature, the effects of two leading interaction terms largely cancel in the case of Σ PES, leading to a significantly reduced interaction. In contrast, in the case of Π PES, the quadrupole term $v_2(R)$ is attractive in the long range (which is probably more typical), similar to the isotropic term $v_0(R)$, which makes the effective interaction stronger (see Fig. S8 of the ESI†). These differences explain why the inelastic cross sections in Fig. 4 are larger in the case of Σ PES compared to Π PES. All higher-order terms (v_4 and above) behave similar on two PESs.

We also noticed that for $j = 0$ the elastic cross section computed by MQCT is in very good agreement with MOLSCAT, in terms of both amplitude and frequency of oscillations and for both Π and Σ PESs. When j is raised, the agreement remains very good in the case of Π PES, but not in the case of Σ PES. To understand the effect of initial rotational excitation of the molecule, we plotted in Fig. S9 and S10 of the ESI† the radial dependence of diagonal matrix elements $M^j_{jm}(R)$ that govern the process of scattering on Π and Σ PESs (see eqn (3)). Fig. S9 (ESI†) shows how matrix elements depend on j (for the same value of $m = 0$), while Fig. S10 (ESI†) shows how the matrix elements depend on m (for the same value of $j = 4$). We found, first of all, that for Π PES the absolute values of matrix elements for the excited rotational states ($j \geq 2$) are larger than that for the ground state $j = 0$, while for Σ PES this is just opposite! Therefore, the molecule + quencher interaction is increased by rotational excitation of the molecule in the case of Π PES, while it is decreased in the case of Σ PES. For example, for $m = 0$ component of the most populated rotational state $j = 4$, the well depth of $M^j_{jm}(R)$ is almost a factor of 4 smaller in the case of Σ PES (~27 cm^{-1}) compared to Π PES (~96 cm^{-1}), as one can see from Fig. S9 (ESI†). However, we also found that increasing the value of quantum number m acts in the opposite direction and reverses the effect of j increase. Namely, in the case of Π PES the well depth of $M^j_{jm}(R)$ is decreased as the value of m is raised (so that $m = 0$ state has the strongest interaction), while in the case of Σ PES the well depth of $M^j_{jm}(R)$ is increased as the value of m is raised (so that $m = 0$ state has the weakest interaction). Due to this trend, $m = 4$ components of $j = 4$ states of Π and Σ PESs exhibit comparable well depths, as one can see from Fig. S10 (ESI†).

Therefore, the variations of j and m have a very significant effect on the molecule–quencher interaction in the case of Σ PES, but only a minor effect in the case of Π PES. This property explains the behavior of cross section oscillations seen in Fig. 2, where in the case of Π PES the oscillations of elastic cross section are insensitive to the rotational excitation of the molecule, while in the case of Σ PES the largest oscillations of elastic cross section are observed for $j = 0$ and are suppressed as the value of j is raised. This happens because the frequency of oscillations is determined by well depth, and the effective well depth of $M^j_{jm}(R)$ decreases with rotational excitation in the case of Σ PES. This trend is seen somewhat better in the full-quantum MOLSCAT calculations but is also present in the MQCT results (see Fig. 2). In Fig. S11 of the ESI,† we have plotted the oscillations of elastic cross sections for individual m-components of $j = 4$ state obtained by MQCT calculations on Π and Σ PESs. We see that the variation of m has an appreciable

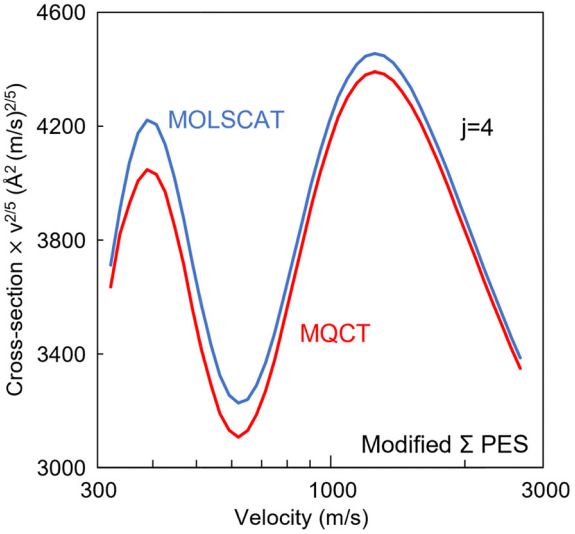

Fig. 6 Velocity-scaled cross sections as a function of O-atom collision velocity calculated using a modified Σ PES for the initial state of $N_2(j = 4)$. The red line is MQCT results and the blue line is MOLSCAT results.

effect on both amplitude and frequency of oscillations in the case of Σ PES, but not so much in the case of Π PES.

At a fundamental level, the oscillations of elastic cross section occur due to the interference term $1 - Ae^{i\delta}$ in eqn (10). The frequency of oscillations is determined by phase δ, which is larger if the molecule–quencher interaction is stronger, while the amplitude of oscillations is determined by the modulus of survival probability amplitude A, which is larger if the inelastic transition probability is smaller. Inelastic transitions are determined by anisotropy of the PES and are weaker in the case of Π PES (check the values of total inelastic cross sections in Fig. 4). Larger inelastic cross sections of Σ PES correspond to smaller survival probability (of the elastic channel), which results in a smaller amplitude of the elastic cross section oscillations (compared to Π PES), as one can see from Fig. 4. As emphasized above, Σ PES of the N_2 + O system is characterized by purely repulsive anisotropic term $v_2(R)$, shown in Fig. S8 (ESI†).

As a numerical experiment, we tried to repeat scattering calculations for Σ PES with the $v_2(R)$ expansion term artificially removed, keeping all other terms intact. Such results for the initial state $j = 4$ are presented in Fig. 6, which can be contrasted against the lower-right frame of Fig. 4. They show that in this case the results of MQCT and MOLSCAT come to an excellent agreement, in terms of both amplitude and frequency of oscillations. When the term $v_2(R)$ is removed from Σ PES, the effective interaction is increased, which increases the frequency of elastic cross section oscillations. At the same time the inelastic transitions are reduced, which increases survival probability amplitude A and leads to larger amplitude of elastic cross section oscillations. All these features are clearly seen in both MQCT and MOLSCAT results presented in Fig. 6.

We can conclude that the properties of Σ PES for N_2 + O (namely, its shallow well combined with strong anisotropy) represent a tough case for MQCT. For this system the MQCT method still gives the oscillations of elastic cross section, but somewhat different from the results of MOLSCAT that predicts oscillations with smaller amplitude and higher frequency. These differences disappear when a more typical PES is used (such as Π PES of N_2 + O) or when the atypical Σ PES of N_2 + O is made more typical (by removing the expansion term responsible for this behavior). During the review of this manuscript the following interpretation was proposed: the properties of the Σ state are determined by weak van der Waals and strongly anisotropic quadrupole–quadrupole contributions, while the Π state, in addition to the above-mentioned contributions, is stabilized by charge transfer. In other words, the character of Σ PES is entirely non-reactive, while Π PES has an additional chemical contribution (and, as shown elsewhere,[17,18] the reactive channels indeed open at higher energies). Most of the ground state PESs describe the reactive process and therefore the behavior of Σ PES might appear unusual, but in fact it is not.

V. Conclusions

In this paper, we explored how the quantum interference effect manifest in the elastic and inelastic scattering channels of the N_2 + O system. Calculations were carried out for two electronic PESs of the system, for several initial rotational states of N_2, in a broad range of N_2 + O collision energies, using three theoretical methods: two versions of the mixed quantum/classical theory (MQCT and AT-MQCT) and the full-quantum coupled-channel method (implemented in MOLSCAT). Overall, state-to-state transition cross-sections for rotational excitation and quenching of N_2 show good agreement between theoretical methods, especially at high energies. Elastic scattering cross-sections are 3–10 times larger compared to inelastic cross-sections and oscillate as a function of energy, which is the result of quantum interference. We found that although the initial rotational excitation of N_2 plays an important role in the individual state-to-state transitions and in the elastic and inelastic scattering processes, the energy dependence of total cross section (elastic + inelastic) appears to be almost insensitive to the initial rotational state of the molecule.

One important phenomenon explored in this study in detail is the dependence of cross section oscillations on the properties of the PES. The PESs for two electronic states of the N_2 + O system used in these calculations are characterized by different well depths and different amounts of angular anisotropy. For Π PES, characterized by a deeper well and a typical anisotropic term, the oscillations of elastic cross section predicted by MQCT are in good agreement with those of MOLSCAT. For Σ PES, characterized by a shallow well and a large anisotropic term, the amplitude and frequency of cross section oscillations predicted by MQCT are somewhat different from those of MOLSCAT.

Using energy dependencies of cross sections for the individual rotational states, we derived the dependence of thermally averaged total cross-section on collision velocity and compared our predictions with experimental data and with the IOS results from the literature. We were able to reproduce experimental data (available at high collision velocities, 800–2200 m s^{-1}) but also demonstrated that the pattern of quantum oscillations

persists through a broad range and expands into low collision velocities, where quantum scattering resonances are common. Both MOLSCAT and MQCT calculations predict a rather regular pattern, with two and a half periods of cross section oscillations in the velocity range 300–3000 m s^{-1} (collision energy range of roughly 30–3000 cm^{-1}). The percent difference between our MQCT method and full quantum MOLSCAT results decreases from $\sim$8% at low energies down to $\sim$2% at high energies. These numbers demonstrate a generally good performance of an approximate MQCT method, and its ability to capture some quantum interference effects.

In the future, our MQCT calculations will be extended to take into consideration the vibrational states of N_2, to explore the rate of $N_2(v = 1)$ ro-vibrational quenching in the upper atmosphere. It should be mentioned, though, that the actual process of $N_2(v = 1)$ quenching in the nature appears to be more complicated than the electronically adiabatic theory presented here. Namely, it was recently demonstrated[17,18] that electronically non-adiabatic transition between Π and Σ PESs, enabled by the vibrational excitation of $N_2(v = 1)$, plays an important role in the quenching process. In order to capture these effects, an extension of MQCT theory into the electronically non-adiabatic realm, and the modification of the MQCT code to handle multiple electronic surfaces with non-adiabatic couplings, would be necessary. This is in principle possible, since the mixed quantum/classical methods are known to work well for electronically non-adiabatic non-reactive molecule + atom collisions.[38]

Conflicts of interest

There are no conflicts to declare.

Acknowledgements

This research was supported by the NSF Chemistry program, under grant number CHE-2102465. We used resources of the National Energy Research Scientific Computing Center, which is supported by the Office of Science of the U.S. Department of Energy under Contract No. DE-AC02-5CH11231. Also, we used HPC resources at Marquette funded in part by the National Science foundation award CNS-1828649. Dr Cecilia Coletti is acknowledged for stimulating discussions and her encouragement of this project. C. Joy acknowledges the support of the Schmitt Fellowship at Marquette. D. Bostan aknowledges the support of the Eisch Fellowship and Bournique Award at Marquette.

References

1 B. Nichols, H. Chadwick, S. D. S. Gordon, C. J. Eyles, B. Hornung, M. Brouard, M. H. Alexander, F. J. Aoiz, A. Gijsbertsen and S. Stolte, Steric effects and quantum interference in the inelastic scattering of NO(X) + Ar, *Chem. Sci.*, 2015, **6**, 2202–2210.

2 X. Shan, C. Xiahou and J. N. L. Connor, Rainbows, supernumerary rainbows and interference effects in the angular scattering of chemical reactions: an investigation using Heisenberg's S matrix programme, *Phys. Chem. Chem. Phys.*, 2018, **20**, 819–836.

3 C. Xiahou, X. Shan and J. N. L. Connor, Rainbows, supernumerary rainbows and interference effects in the angular scattering of chemical reactions: effect of varying the modulus of the S matrix in the context of Heisenberg's S matrix programme, *Phys. Scr.*, 2019, **94**, 65401.

4 C. Xiahou and J. N. L. Connor, Glories, hidden rainbows and nearside–farside interference effects in the angular scattering of the state-to-state H + HD $\rightarrow$ H_2 + D reaction, *Phys. Chem. Chem. Phys.*, 2021, **23**, 13349–13369.

5 B. K. Kendrick, H. Li, M. Li, S. Kotochigova, J. F. E. Croft and N. Balakrishnan, Non-adiabatic quantum interference in the ultracold Li + LiNa $\rightarrow$ Li_2 + Na reaction, *Phys. Chem. Chem. Phys.*, 2021, **23**, 5096–5112.

6 M. Besemer, G. Tang, Z. Gao, A. van der Avoird, G. C. Groenenboom, S. Y. T. van de Meerakker and T. Karman, Glory scattering in deeply inelastic molecular collisions, *Nat. Chem.*, 2022, **14**, 664–669.

7 J. N. L. Connor, Theory of forward glory scattering for chemical reactions, *Phys. Chem. Chem. Phys.*, 2004, **6**, 377–390.

8 C. Xiahou and J. N. L. Connor, Theory of forward glory scattering for chemical reactions: accuracy of semiclassical approximations using a J-shifted Eckart parameterization for the scattering matrix element, *Mol. Phys.*, 2006, **104**, 159–175.

9 B. Brunetti, G. Liuti, E. Luzzatti, F. Pirani and F. Vecchiocattivi, Study of the interactions of atomic and molecular oxygen with O2 and N2 by scattering data, *J. Chem. Phys.*, 1981, **74**, 6734–6741.

10 D. Cappelletti, M. Bartolomei, F. Pirani and V. Aquilanti, Molecular Beam Scattering Experiments on Benzene- Rare Gas Systems: Probing the Potential Energy Surfaces for the C_6H_6 - He, -Ne, and -Ar Dimers, *J. Phys. Chem. A*, 2002, **106**, 10764–10772.

11 F. Pirani, S. Brizi, L. F. Roncaratti, P. Casavecchia, D. Cappelletti and F. Vecchiocattivi, Beyond the Lennard-Jones model: a simple and accurate potential function probed by high resolution scattering data useful for molecular dynamics simulations, *Phys. Chem. Chem. Phys.*, 2008, **10**, 5489–5503.

12 D. Cappelletti, A. Bartocci, F. Grandinetti, S. Falcinelli, L. Belpassi, F. Tarantelli and F. Pirani, Experimental evidence of chemical components in the bonding of helium and neon with neutral molecules, *Chem. – Eur. J.*, 2015, **21**, 6234–6240.

13 F. Nunzi, D. Cesario, L. Belpassi, F. Tarantelli, L. F. Roncaratti, S. Falcinelli, D. Cappelletti and F. Pirani, Insight into the halogen-bond nature of noble gas-chlorine systems by molecular beam scattering experiments, ab initio calculations and charge displacement analysis, *Phys. Chem. Chem. Phys.*, 2019, **21**, 7330–7340.

14 A. Bergeat, J. Onvlee, C. Naulin, A. van der Avoird and M. Costes, Quantum dynamical resonances in low-energy

CO (j = 0) + He inelastic collisions, *Nat. Chem.*, 2015, **7**, 349–353.

15 S. N. Vogels, T. Karman, J. Kłos, M. Besemer, J. Onvlee, A. van der Avoird, G. C. Groenenboom and S. Y. T. van de Meerakker, Scattering resonances in bimolecular collisions between NO radicals and H_2 challenge the theoretical gold standard, *Nat. Chem.*, 2018, **10**, 435–440.

16 B. Mandal, A. Semenov and D. Babikov, Calculations of differential cross sections using mixed quantum/classical theory of inelastic scattering, *J. Phys. Chem. A*, 2018, **122**, 6157–6165.

17 Q. Hong, M. Bartolomei, F. Esposito, C. Coletti, Q. Sun and F. Pirani, Reconciling experimental and theoretical vibrational deactivation in low-energy O + N_2 collisions, *Phys. Chem. Chem. Phys.*, 2021, **23**, 15475–15479.

18 Q. Hong, M. Bartolomei, F. Pirani, F. Esposito, Q. Sun and C. Coletti, Vibrational deactivation in $O(^3P)$ + N_2 collisions: from an old problem towards its solution, *Plasma Sources Sci. Technol.*, 2022, **31**, 84008.

19 R. Celiberto, I. Armenise, M. Cacciatore, M. Capitelli, F. Esposito, P. Gamallo, R. K. Janev, A. Laganà, V. Laporta, A. Laricchiuta, A. Lombardi, M. Rutigliano, R. Sayós, J. Tennyson and J. M. Wadehra, Atomic and molecular data for spacecraft re-entry plasmas, *Plasma Sources Sci. Technol.*, 2016, **25**, 33004.

20 T. Schönherr, K. Komurasaki, F. Romano, B. Massuti-Ballester and G. Herdrich, Analysis of Atmosphere-Breathing Electric Propulsion, *IEEE Trans. Plasma Sci.*, 2015, **43**, 287–294.

21 J. M. Hutson and C. R. le Sueur, MOLSCAT: a program for non-reactive quantum scattering calculations on atomic and molecular collisions, *Comput. Phys. Commun.*, 2019, **241**, 9–18.

22 J. M. Hutson and R. le Sueur, *MOLSCAT: a program for non-reactive quantum scattering calculation on atomic and molecular collisions, Version 2022.0*, 2022.

23 G. D. Billing, The semiclassical treatment of molecular roto/vibrational energy transfer, *Comput. Phys. Rep.*, 1984, **1**, 239–296.

24 G. D. Billing, *The quantum classical theory*, Oxford University Press, New York, 2003.

25 T. V. Markova, A. A. Aksenov, S. V. Zhluktov, D. V. Savitsky, A. D. Gavrilov, E. E. Son and A. N. Prokhorov, *J. Phys.: Conf. Ser.*, 2016, **774**, 12095.

26 M. Kh Gadzhiev, Y. M. Kulikov, V. A. Panov, E. E. Son and A. S. Tyuftyaev, Supersonic plasmatron nozzle profiling with the real properties of high temperature working gas, *High Temp.*, 2016, **54**, 38–45.

27 T. V. Markova, A. A. Aksenov, S. V. Zhluktov, D. V. Savitskiy, A. D. Gavrilov and E. E. Son, Numerical simulation of gas flow past scale model of hypersonic vehicle in wind tunnel, *High Temp.*, 2017, **55**, 280–285.

28 A. Semenov, B. Mandal and D. Babikov, MQCT: User-ready program for calculations of inelastic scattering of two molecules, *Comput. Phys. Commun.*, 2020, **252**, 107155.

29 B. Mandal, C. Joy, D. Bostan, A. Eng and D. Babikov, Adiabatic Trajectory Approximation: A New General Method in the Toolbox of Mixed Quantum/Classical Theory for Collisional Energy Transfer, *J. Phys. Chem. Lett.*, 2023, **14**, 817–824.

30 A. Semenov and D. Babikov, Mixed quantum/classical approach for description of molecular collisions in astrophysical environments, *J. Phys. Chem. Lett.*, 2015, **6**, 1854–1858.

31 A. Semenov and D. A. Babikov, MQCT. I. Inelastic Scattering of Two Asymmetric-Top Rotors with Application to H_2O+ H_2O, *J. Phys. Chem. A*, 2017, **121**, 4855–4867.

32 B. Mandal, C. Joy, A. Semenov and D. Babikov, Mixed Quantum/Classical Theory for Collisional Quenching of PAHs in the Interstellar Media, *ACS Earth Space Chem.*, 2022, **6**, 521–529.

33 B. Mandal and D. Babikov, Rate coefficients for rotational state-to-state transitions in H_2O + H_2O collisions for cometary and planetary applications, as predicted by mixed quantum-classical theory, *Astron. Astrophys.*, 2023, **671**, A51.

34 C. Boursier, B. Mandal, D. Babikov and M. L. Dubernet, New H_2O–H_2O collisional rate coefficients for cometary applications, *Mon. Not. R. Astron. Soc.*, 2020, **498**, 5489–5497.

35 B. Mandal, A. Semenov and D. Babikov, Adiabatic Trajectory Approximation within the Framework of Mixed Quantum/Classical Theory, *J. Phys. Chem. A*, 2020, **124**, 9877–9888.

36 A. Semenov and D. Babikov, Mixed quantum/classical theory of rotationally and vibrationally inelastic scattering in space-fixed and body-fixed reference frames, *J. Chem. Phys.*, 2013, **139**, 174108.

37 A. Semenov and D. Babikov, Mixed quantum/classical calculations of total and differential elastic and rotationally inelastic scattering cross sections for light and heavy reduced masses in a broad range of collision energies, *J. Chem. Phys.*, 2014, **140**, 44306.

38 D. Babikov, F. Aguillon, M. Sizun and V. Sidis, Fragmentation of Na^{2+} dimer ions in kilo-electron-volt collisions with He: A coupled wave-packet study, *Phys. Rev. A: At., Mol., Opt. Phys.*, 1999, **59**, 330.

